Characterization of the amorphous metallic alloy $Al_{85}Ni_{10}Sm_5$

Caracterização da liga metálica amorfa $Al_{85}Ni_{10}Sm_5$

Marcelo Lemos da Silva[†], Lucas Correa Campos, Luis César Rodríguez Aliaga, Ivan Napoleão Bastos, Alexandre Melhorance Barboza

Instituto Politécnico, Universidade do Estado do Rio de Janeiro, Nova Friburgo, RJ, Brasil
[†]**Corresponding author:** mlsilva@iprj.uerj.br

Abstract

Aluminum alloys are highly significant materials in the industry due to their excellent mechanical properties and corrosion resistance. These alloys are widely used in various applications in the automotive and aerospace industries. The addition of alloying elements such as nickel, copper, and magnesium allows for different combinations of properties, which makes the alloys more versatile. Among aluminum alloys, the amorphous alloys studied in this work have received increasing attention due to their unique properties. Additionally, there is a limited amount of research on these materials, unlike the numerous studies already conducted on conventional crystalline structure alloys. In this work, the metallic alloy with the atomic composition $Al_{85}Ni_{10}Sm_5$ and an amorphous structure, produced by melt-spinning, was structurally, thermally, and electrochemically characterized. The structural and thermal characterization was performed using X-ray diffraction (XRD), scanning electron microscopy (SEM), and differential scanning calorimetry (DSC) techniques to confirm its amorphous nature. The electrochemical characterization was carried out through open circuit and potentiodynamic polarization tests in an aqueous medium with 3.5% mass NaCl at room temperature. The results indicate that the fully amorphous alloy is of the glassy type, with $Tg = 522$ K, and exhibits low thermal stability ($\Delta Tx = 16$ K). The electrochemical tests show a corrosion potential of approximately -520 mV relative to the saturated calomel reference electrode, suggesting that the amorphous alloy is more corrosion-resistant than pure aluminum in its crystalline state.

Keywords

Amorphous Al-Ni-Sm Alloy • Physical characterization • Electrochemical characterization

Resumo

As ligas de alumínio são materiais de grande relevância na indústria devido às suas excelentes propriedades mecânicas e resistência à corrosão. Estas ligas são amplamente utilizadas em diversas aplicações na indústria automotiva e aeroespacial. A adição de elementos de liga, como níquel, cobre e magnésio, permite a obtenção de diferentes combinações de propriedades, o que torna as ligas mais versáteis. Dentre as ligas de alumínio, as ligas amorfas, estudadas neste trabalho, têm recebido atenção crescente devido às suas propriedades únicas. Além disso, há uma quantidade limitada de estudos sobre esses materiais, ao contrário dos numerosos estudos já realizados para as ligas convencionais com estrutura cristalina. Neste trabalho, a liga metálica de composição atômica $Al_{85}Ni_{10}Sm_5$ com estrutura amorfa, produzida por melt-spinning, foi caracterizada estrutural, térmica e eletroquimicamente. A caracterização estrutural e térmica foi realizada por meio de técnicas de difração de raios-X (DRX), microscopia eletrônica de varredura (MEV) e calorimetria diferencial exploratória (DSC) para

comprovar sua natureza amorfa. A caracterização eletroquímica foi realizada por ensaios de circuito aberto e polarização potenciodinâmica, em meio aquoso com 3,5% em massa de NaCl a temperatura ambiente. Os resultados indicam que a liga totalmente amorfa é do tipo vítrea, com Tg = 522 K, e apresenta baixa estabilidade térmica (ΔTx = 16 K). Os ensaios eletroquímicos mostram um potencial de corrosão de aproximadamente -520 mV em relação ao eletrodo de calomelano saturado, sugerindo que a liga amorfa é mais resistente à corrosão que o alumínio puro em seu estado cristalino.

Palavras-chave

Liga Amorfa de Al-Ni-Sm • Caracterização física • Caracterização eletroquímica

1 Introduction

It is known that technological and industrial advancement largely depends on the development of new materials with improved physical and mechanical properties compared to those currently available [1]. With environmental issues being increasingly discussed, the need to seek more sustainable solutions for the environment is evident [2-4].

When we think about sustainable energy, sources such as wind and solar come to mind. However, several other forms of green energy are being widely studied. Among them, we can mention hydrogen storage [5-7], liquid metal batteries [8], and lithium batteries [9]. All energy generation or storage devices require materials that enable miniaturization and weight reduction of their components [10].

In this context, the development of materials with an amorphous structure stands out [11,12]. Theoretically, these metastable materials often present physical and mechanical properties superior to those of their crystalline counterparts. It is therefore essential to test this hypothesis to predict their possible technological applications [13,14].

Recent research has focused on the analysis of new materials, including amorphous aluminum-based alloys, which, due to their unique structure and low density, are well-suited for various applications [15-19]. Thus, the main goal of this study is to investigate the electrochemical behavior of the amorphous aluminum-based alloy, $Al_{85}Ni_{10}Sm_5$, produced by the melt-spinning technique, to better understand its behavior when exposed to an environment similar to seawater. The thermodynamics potential-pH diagrams in pure water of the three elements, aluminum, nickel, and samarium are shown in Figure 1. At neutral pH and water stability region, the thermodynamics predicts that aluminum and nickel are in passive state, while samarium shows corrosion, even in absence of chloride. The relation between standard hydrogen electrode (SHE) and saturated calomel electrode (SCE) is given by $E_{SHE} = E_{SCE} + 0.244\ (V)$. The colored regions in the diagrams correspond to immunity.

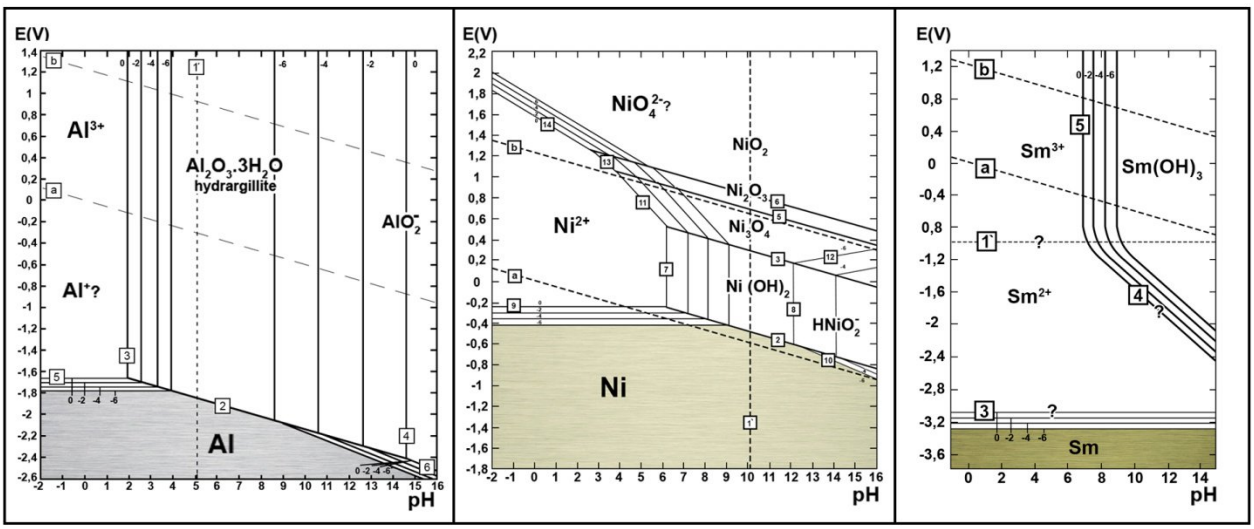

Figure 1: Thermodynamic potential-pH diagrams for aluminum (Al), nickel (Ni), and samarium (Sm) in pure water at 298 K and 1 atm. Colored regions correspond to immunity. Adaptation from Pourbaix [20].

This study aims to employ X-ray diffraction (XRD), scanning electron microscopy (SEM), differential scanning calorimetry (DSC), and electrochemical techniques to characterize the amorphous alloy $Al_{85}Ni_{10}Sm_5$. The alloy in

question was examined in terms of structural, thermal, and electrochemical aspects to confirm its amorphous nature and understand its stability and corrosion resistance. The study simulated seawater conditions with a 3.5% NaCl solution, observing the alloy's behavior upon exposure to chloride ions. Additionally, the work aims to evaluate the thermal stability and crystallization tendency of the alloy and compare its corrosion resistance with corresponding crystalline state alloys.

2 Materials and methods

The entire manufacturing process of the $Al_{85}Ni_{10}Sm_5$ alloy, both with crystalline and amorphous structures, was carried out at the Department of Materials Engineering of the Federal University of São Carlos (São Carlos/SP), including the respective structural and thermal characterizations. Sample preparation and tests for electrochemical characterization were conducted at the Corrosion Laboratory of the Polytechnic Institute of Rio de Janeiro State University (Nova Friburgo/RJ).

2.1 Processing of Crystalline Metallic Alloy

To obtain the alloy with a crystalline structure, an arc-melting furnace (Arc-Melter, Hechingen D72329) was used. This device was equipped with a non-consumable tungsten electrode, a melting chamber with an inert high-purity argon atmosphere, and a water-cooled copper crucible, as shown in Figure 2.

Figure 2: Electric Arc- Melter furnace Hechingen D72329 Buhler (DEMa/UFSCar).

The alloy was melted in an ultra-pure argon atmosphere, with previous melting of Ti-getter to eliminate residual air molecules. This stage of the alloy preparation is crucial because slight changes in composition and the presence of oxygen can significantly affect the ability to achieve the desired amorphous structure. The base elements used in this study were high purity electrolytic elements. Nominal purity and morphology are shown in Table 1. The mass balance was adjusted to produce an alloy with atomic composition of $Al_{85}Ni_{10}Sm_5$.

Table 1: Purity and morphology of the elements used in the alloy preparation.

Element	Purity	Morphology
Aluminum (Al)	99.995%	Square ingot
Nickel (Ni)	99.999%	Cylindrical bar
Samarium (Sm)	99.900%	Pieces with cubic morphology

Initially, the elements were weighed and chemically cleaned (process for removing surface oxides) in acidic solutions. They were then washed with acetone using ultrasonic agitation for 10 minutes. It is important to highlight that samarium, due to its high chemical reactivity with acids, was not pickled, being only subjected to surface cleaning with a steel brush.

After cleaning and weighing, the materials were placed in the furnace chamber and melted according to their respective melting temperatures. For Al-Ni-Sm alloys, aluminum, which has the lowest melting point among the

alloy elements, was positioned in the lower part of the furnace to avoid premature melting and mass losses. Next, samarium was added, followed by nickel, with the aim of first melting the element least reactive to oxygen. Before melting, the melt chamber was evacuated to *ca*. 10^{-8} atm and filled with ultra-pure argon to 0.5 atm by three times. A final cleaning was carried out and the chamber was filled with argon to a pressure of 0.9 atm. Then, the residual oxygen was eliminated by melting and cooling the Ti-getter at least three times. Finally, the metals were melted to form a single ingot, which was turned and remelted at least five times to ensure chemical homogeneity. After preparing the ingots, the samples were weighed again, finding that the maximum mass loss was approximately 0.05%, an acceptable value.

2.2 Preparation of Amorphous Ribbons

The ribbons were manufactured using melt-spinning equipment (Model D7400 from Tübingen) at the Laboratory of Amorphous and Nanocrystalline Materials at DEMa/UFSCar, as shown in Figure 3.

Figure 3: Melt-spinning equipment, model D7400 from Tübingen (DEMa/UFSCar).

Ingots weighing approximately 25 g, corresponding to the alloy, previously prepared in the arc-melter, were placed in a quartz crucible. The crucible was previously pickled with a 1% HF aqueous solution, degreased, and internally coated on the cylindrical part with boron nitride (BN) to prevent reactions between the alloy and the crucible at high temperatures.
The crucible had a leak hole with a diameter of 1.0 mm. Before melting, the melt-spinning chamber was evacuated to *ca*. 10^{-8} atm and filled with ultrapure argon to 0.26 atm, repeating this procedure five times. The final pressure used was 0.39 atm and the ejection pressure was 0.66 atm, resulting in an overpressure of 0.26 atm. The tangential velocity of the copper wheel and the pouring temperature were approximately 25 m/s and 473 K above the alloy's liquidus temperature.

2.3 Structural and Thermal Characterization of Amorphous Ribbons

The melt spun ribbon samples, processed by melt-spinning, were structurally analyzed using X-ray diffraction. The tests were carried out on a Siemens D5005 diffractometer, with Cu-Kα radiation, current of 40 mA and voltage of 40 V. The scan was performed at a rate of 0.2 ° per minute over a 2θ range of 20 ° to 90 °. For scanning electron microscopy (SEM) examination, a Philips scanning electron microscope, model XL-30 FEG, equipped with a Buehler X-ray energy dispersion spectrometer was used.

The thermal characterization of the crystalline samples was conducted through differential thermal analysis (DTA), using Netzsch DSC 404 equipment, with a heating rate of 0.33 K/s until reaching a temperature of 1573 K, using alumina (Al_2O_3) crucibles. As for the amorphous samples, the analysis was carried out with a DSC 200 F3 Maia calorimeter, using a heating rate of 0.6 K/s in the temperature range of 293 to 893 K. All the experiments were performed under an ultrapure argon atmosphere. The methodology used consisted of two heating-cooling runs to clearly determine the transitions associated with different thermally activated phenomena, such as T_g, T_x and T_l.

2.4 Electrochemical Characterization

To carry out the electrolytic experiments, the amorphous ribbons were cut so that the exposed face resulted in an area of 50 mm². An anti-corrosive insulating tape was used to isolate the other side of the tape, in order to only expose the area of interest, such as displayed in figure 4(a). All the samples were sanded with 2500 grit water sandpaper. During sanding, the sample was fixed at one end to a glass plate and sanded approximately 30 times on the face. The electrolyte used was a solution of distilled water with 3.5% NaCl, to simulate the alloy's behavior in a marine environment. All the electrochemical tests were conducted at room temperature, approximately 298 K. The potentiostat used was a Gamry Instruments, Reference 600, a saturated calomel reference electrode (SCE) and a spiral platinum wire as a counter electrode. The test setup scheme can be seen in figure 4(b). The polarization curves were initiated at a potential 50 mV below the corrosion potential and terminated at -0.2 V versus the Saturated Calomel Electrode (SCE).

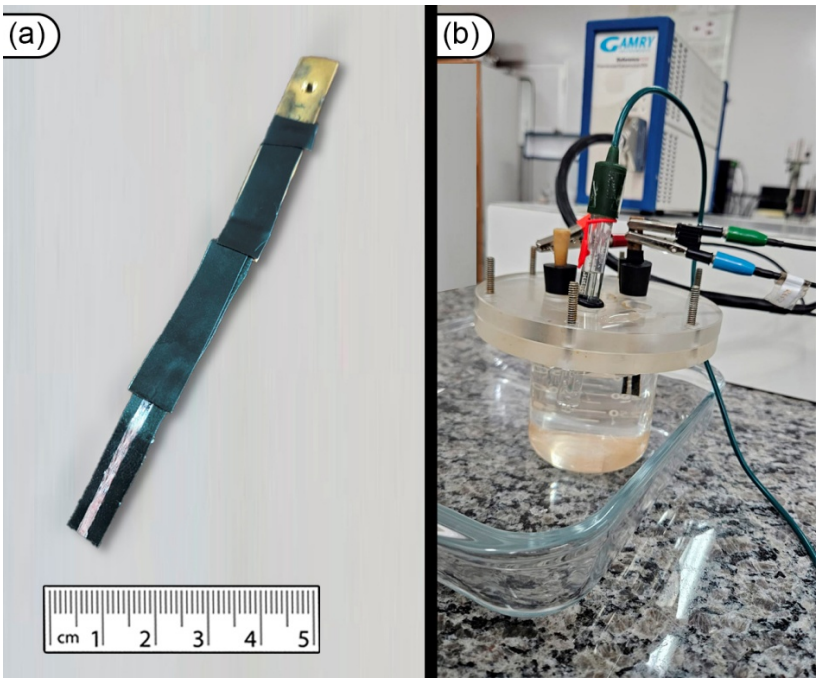

Figure 4: (a) Melt spun-ribbon amorphous sample, (b) Electrochemical test setup.

3 Results and Discussion

In this section, the results of the structural, thermal, and chemical characterization are presented and discussed. These include X-ray diffraction (XRD), scanning electron microscopy (SEM), and differential scanning calorimetry (DSC) analysis. Finally, the results of the electrochemical tests are considered.

3.1 Structural and Thermal Characterization

The first consideration in this study was to determine if the melt-spun ribbon presents an atomic amorphous organization, thus, small pieces of ribbon were submitted to analysis by XRD. Figure 5 shows the XRD pattern in an angular range from 20 to 90 º, obtained under irradiation of copper source.

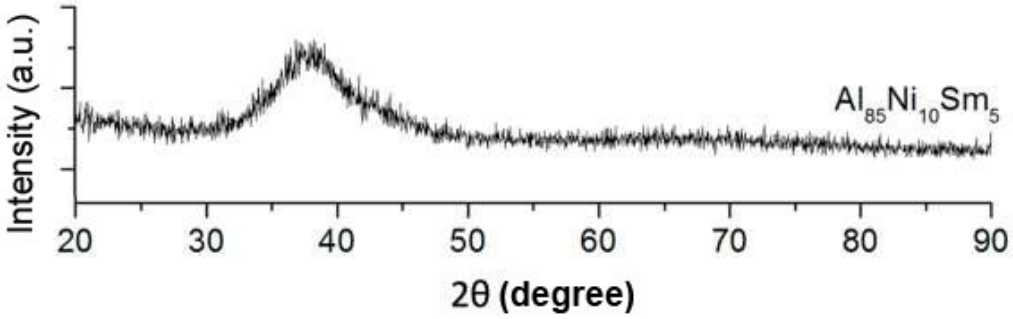

Figure 5: X-ray diffractograms of the samples.

It can be observed that the sample exhibits the typical profile of an amorphous phase, characterized by an wide halo around $2\theta = 38.6$ °, an expected result according to the literature [21,22]. There is no presence of crystalline phase peaks superimposed on the amorphous diffractogram. Thus, it is concluded that the sample under study is completely amorphous, although it is possible that a certain fraction of nanometer-sized crystals is immersed in the amorphous matrix. However, these nanocrystals were not detected by XRD. With this we can move on to the next steps, knowing that the process of obtaining the amorphous alloy was successful.
In order to have a complete picture of the structural characteristics of the melt-spun ribbon, samples of ribbon were analyzed by SEM under the backscattered electron (BSE) mode. The ribbon has only the amorphous phase, as can be seen on the microphotograph in Figure 6, corroborating the findings from XRD.

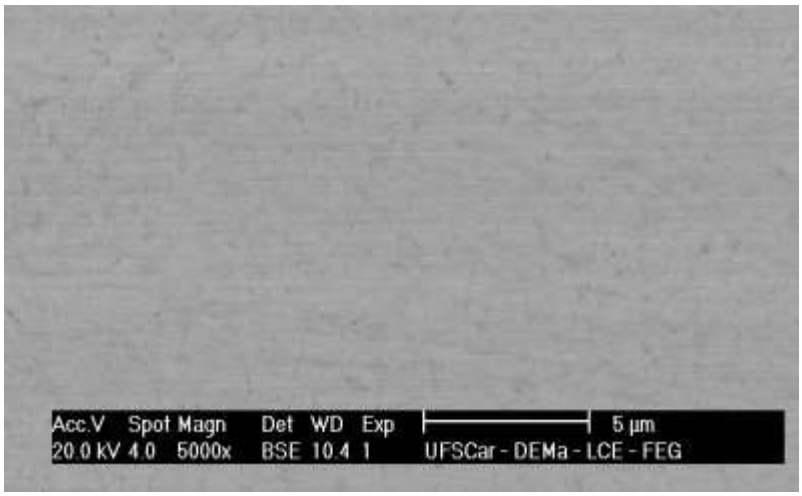

Figure 6: SEM micrograph – BSE of the amorphous $Al_{85}Ni_{10}Sm_5$ alloy ribbon.

It is worthy note that the BSE technique provides a chemical rather than a topological contrast [23]. Furthermore, the overall analysis of the chemical composition of the amorphous ribbon by EDS showed that the chemical composition is quite close to the nominal composition, with only a small discrepancy of approximately 0.3 atom percent for aluminum. Therefore, it can be stated that there was no systematic loss of aluminum in the melt spun ribbon manufacturing process, and the greatest loss possibly occurred during the processing of the ingots in the arc furnace, technically validating the alloy obtained.

Table 2 presents the values of the atomic percentages of the chemical elements present in the amorphous alloy. It should be noted that the results obtained by EDS have an error of up to 5%, as it is a semi-quantitative technique and a statistical measurement of the material. To carry out the test, the spectrometer was previously calibrated with a high-purity nickel sample. These values indicate that the composition is close to the nominal one, suggesting that this loss does not significantly affect the glass forming ability (GFA) of the alloy.

Table 2: Atomic percentage of alloying elements by EDS.

Element	EDS	Nominal
Al	84 ± 1	85
Ni	9.98 ± 0.02	10
Sm	4.99 ± 0.03	5
O	0.03 ± 0.01	0

Observing table 2, aluminum is the element that presents a greater deviation in relation to the nominal composition. This deviation is mainly related to the loss of aluminum during the processing of the crystalline ingot in the arc-melter furnace. That deviation is observed in all aluminum-based alloys because the melting temperature of aluminum is relatively low ($T_m = 1033$ K) when compared to that of nickel ($T_m = 1728$ K) and samarium ($T_m = 1345$ K).

On the other hand, is widely known that differential thermal analysis (DTA) is a proper technique to determine the melting temperature of the alloys. Thus, this technique was applied to precisely determine the liquidus temperature of the $Al_{85}Ni_{10}Sm_5$ alloy, under crystalline structure, founding a value of approximately 1433 K. A complementary technique widely used in the study of amorphous materials is differential scanning calorimetry (DSC). Figure 6 shows the DSC thermogram at a heating rate of 0.6 K/s, where can be seen a clear endothermic event due to glass transition (T_g), and several exothermal peaks due to different types of crystallization. Figure 7 shows only the onset of crystallization (T_x).

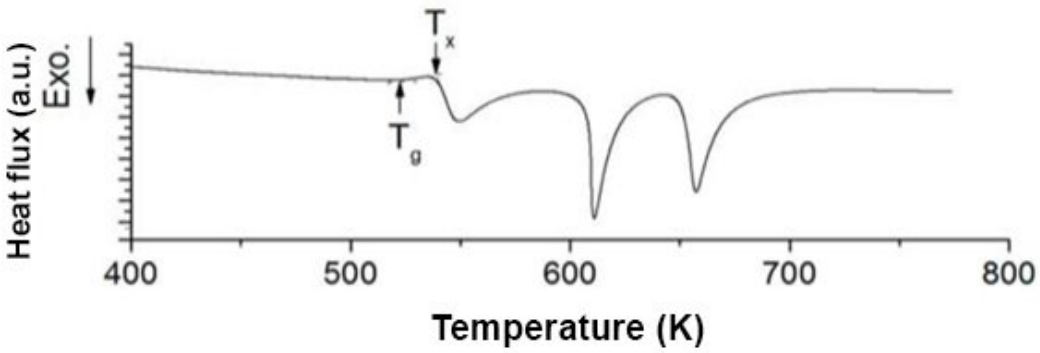

Figure 7: DSC thermogram obtained at a heating rate of 40 K/min on the amorphous ribbon.

To improve the quality of DSC curves, two subsequent measurements were performed under the same conditions. On the first run, one can obtain all the thermal events due to characteristics of the samples. However, on the second run, just a simple curve without transition is expected which is known as base line. The difference between both obtained signals allows obtaining an improved curve where the thermal events are very clear and free of external interferences.

3.2 Electrochemical measurements

Figure 8 shows the open circuit potential (Eocp) curve as a function of time for the $Al_{85}Ni_{10}Sm_5$ alloy. Although neither surface chemical testing nor near-surface solution content testing was performed, the correlation between the initial oscillations observed in the open circuit potential and the thermodynamic stability at pH 6.5 [20] suggests that samarium dissolves into Sm^{3+} ion, part of the nickel also dissolves to form Ni^{2+}, and the remaining aluminum forms hydrargillite ($Al_2O_3.3H_2O$) on the surface. Thus, the initial potential fluctuations correspond to the dissolution of Sm and Ni and the passivation of Al, with the corrosion potential stabilizing around -500 mV vs SCE. The potential drops are likely related to the dissolution and the depart of atoms from the surface, exposing bare aluminum, which progressively passivates with potential increase.

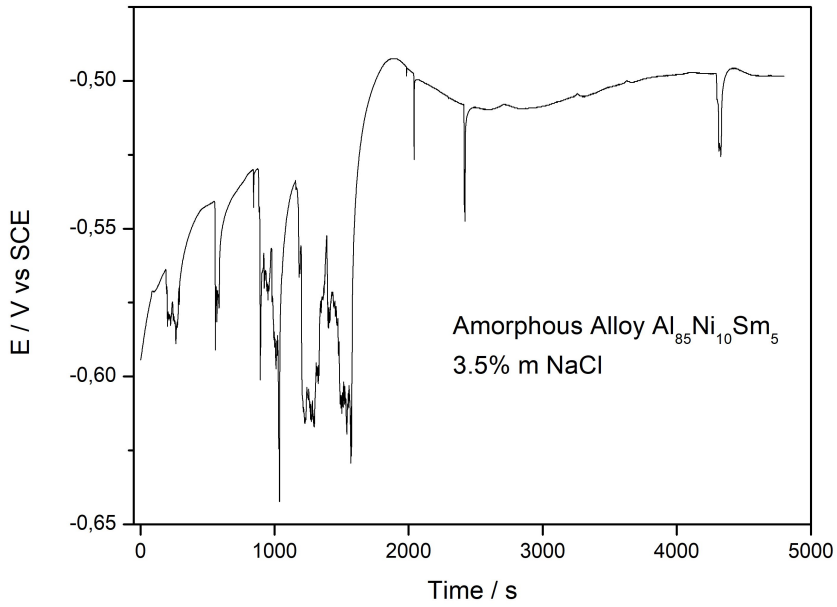

Figure 8: Open circuit potential of melt spun ribbon immersed in aqueous electrolyte.

Figure 9 shows the polarization curves of the $Al_{85}Ni_{10}Sm_5$ amorphous alloy samples. At potentials above the corrosion potential, within a small potential range the surface tends to passivate. However, relatively large anodic peaks occur. These peaks are large then are not caused by metastable pits, but likely to dissolution of nickel and samarium. In the literature, the average value of pure aluminum in 0.1 mol/L NaCl is -0.67 V vs SCE [24], which is below the range of figure 9, i.e., the polarization occurs under pitting susceptibility. The present corrosion potential is higher than other studies of crystalline samples [25], and this fact maybe caused by the amorphous structure.

On aluminum surfaces, chloride ions play a particularly aggressive role in intensifying corrosion by interacting with the passive oxide film that is typically only a few nanometers thick. Diverse interactions with the passive film, such as the adsorption of Cl^- on the surface of the passive oxide, incorporation of Cl^- into the film, possible substitution of O^{2-} by Cl^- in the film, and oxide thinning, as well as other phenomena that are not completely consensual [24], contribute to the increased corrosion process.

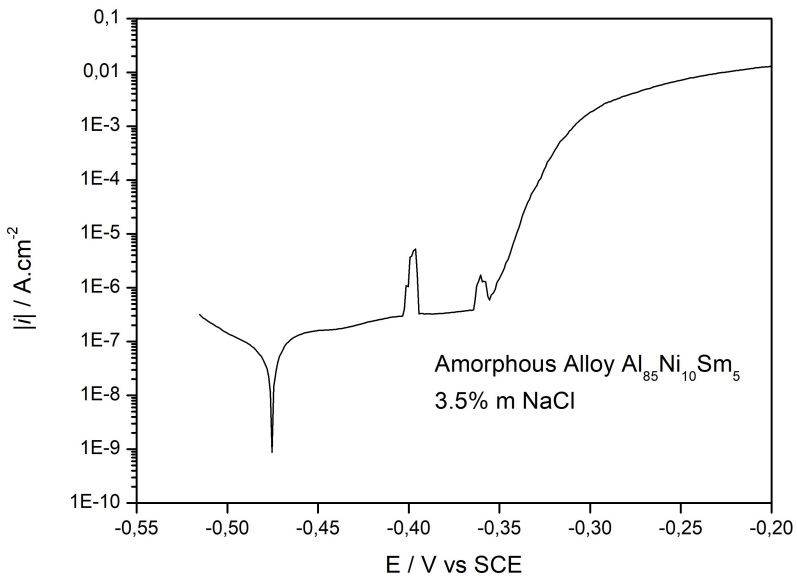

Figure 9: Potentiodynamic polarization curve.

4 Conclusions

The $Al_{85}Ni_{10}Sm_5$ alloy under melt spun ribbon shape was analyzed by using X-ray diffraction (XRD), scanning electron microscopy (SEM), Differential scanning calorimetry (DSC), and electrochemical techniques. These techniques proved to be extremely valuable and successfully achieved the main objective of characterizing thin samples.

The XRD results show the formation of an elongated halo at $2\theta = 38.6$ °, with no observable crystalline phase peaks. Therefore, it can be concluded that the sample under study is fully amorphous. This finding is further confirmed by the SEM analysis, where no secondary phases are observed.

The thermal analysis of the crystalline alloy indicated a pseudo-eutectic behavior with a liquidus temperature around of 1433 K. The DSC thermogram provided the T_g and T_x temperatures characteristic of the amorphous phase, allowing the determination of the supercooled liquid region ($\Delta T_x = 16$ K), which indicates that the amorphous phase is not very stable against thermal crystallization.

Electrochemical techniques show that the corrosion potential of the studied amorphous alloy is approximately -0.52 V vs SCE. Thus, at the corrosion potential and pH 6.5, only aluminum would be in the passive state, according to Pourbaix diagrams. The polarization techniques indicate intense dissolution of the sample at anodic potentials due to the abrupt increase in current. Comparing this with the Pourbaix diagrams of aluminum, nickel, and samarium in water, and considering the pH of the electrolyte used, aluminum should be in a passivated state. Therefore, it can be considered that the local pH under anodic polarization must be at least 5.0 for all alloy components to dissolve.

Acknowledgments

The authors express their gratitude to FAPERJ (Fundação Carlos Chagas Filho de Amparo à Pesquisa do Estado do Rio de Janeiro) for the financial support, as well as to CNPq and InovUerj for their assistance through the Qualitec scholarship within the project (ML Silva). This research was partially funded by the Coordenação de Aperfeiçoamento de Pessoal de Nível Superior – Brasil (CAPES) – Finance Code 001.

References

[1] E. V. da Costa, M. L. da Silva, M. P. M. de Carvalho, D. M. da Cruz, L. C. R. Aliaga, and I. N. Bastos, “Electrochemical characterization of amorphous and crystalline NI62NB38 and NI59.24NB37.76B3.00 alloys,” *VETOR - Revista de Ciências Exatas e Engenharias*, vol. 34, no. 1, pp. 119–129, 2024. Available at: https://doi.org/10.14295/vetor.v34i1.17711

[2] H. Mumtaz, M. Farhan, M. Amjad, F. Riaz, Ali H. Kazim, M. Sultan, M. Farooq, M.A. Mujtaba, I. Hussain, M. Imran, S. Anwar, A. M. El-Sherbeeny, F. A. Siddique, S. Armaković, Q. Ali, I. A. Chaudhry, and A. Pettinau, “Biomass waste utilization for adsorbent preparation in CO_2 capture and sustainable environment applications,” *Sustainable Energy Technologies and Assessments*, vol. 46, p. 101288, 2021. Available at: https://doi.org/10.1016/j.seta.2021.101288

[3] M. Farooq, M. E. M. Soudagar, M. Imran, M. Arslan, M. S. Tariq, A. Pettinau and J. M. Andresen, “Carbon capture for sustainable environment in developing countries,” In: M. Asif (eds) *Energy and Environmental Security in Developing Countries*. Advanced sciences and technologies for security applications, Springer, Cham, 2021. Available at: https://doi.org/10.1007/978-3-030-63654-8_21

[4] X. Piao and S. Managi, “Global evaluation of the natural environment and household income for sustainable development,” *Sustainable Futures*, vol. 8, p. 100254, 2024. Available at: https://doi.org/10.1016/j.sftr.2024.100254

[5] B. He, Y. Lu, J. Jiang, Z. Zhan, B. Ni, L. Lv, and T. Pan, “Comprehensive hydrogen storage properties of free-V Ti1-Zr Mn0.9Cr07Fe0.1 alloys with different Zr substitution content,” *Progress in Natural Science: Materials International*, in press, 2024. Available at: https://doi.org/10.1016/j.pnsc.2024.07.011

[6] J. Zhu, H. Liu, J. Kong, J. Wang, W. Ji, Z. Wei, X. Yao, and X. Wang, "Exploring hydrogen storage safety research by bibliometric analysis," *International Journal of Hydrogen Energy*, vol. 81, pp. 27–39, 2024. Available at: https://doi.org/10.1016/j.ijhydene.2024.07.285

[7] A. G. Olabi, A. S. Bahri, A. A. Abdelghafar, A. Baroutaji, E. T. Sayed, A. H. Alami, H. Rezk, and M. A. Abdelkareem, "Large-scale hydrogen production and storage technologies: Current status and future directions," *International Journal of Hydrogen Energy*, vol. 46, no. 45, pp. 23498–23528, 2021. Available at: https://doi.org/10.1016/j.ijhydene.2020.10.110

[8] Q. Zeng, Z. Lv, S. Li, B. Yang, J. He, and J. Song, "Electrolytes for liquid metal batteries," *Materials Research Bulletin*, vol. 170, p. 112586, 2024. Available at: https://doi.org/10.1016/j.materresbull.2023.112586

[9] H. Niu, N. Zhang, Y. Lu, Z. Zhang, M. Li, J. Liu, N. Zhang, W. Song, Y. Zhao, and Z. Miao, "Strategies toward the development of high-energy-density lithium batteries," *Journal of Energy Storage*, vol. 88, p. 111666, 2024. Available at: https://doi.org/10.1016/j.est.2024.111666

[10] N. Nasajpour-Esfahani, H. Garmestani, M. Bagheritabar, D. J. Jasim, D. Toghraie, S. Dadkhah, and H. Firoozeh, "Comprehensive review of lithium-ion battery materials and development challenges," *Renewable and Sustainable Energy Reviews*, vol. 203, p. 114783, 2024. Available at: https://doi.org/10.1016/j.rser.2024.114783

[11] M. Metikoš-Huković, Z. Grubač, R. Babić, and N. Radić, "Corrosion resistance of amorphous aluminium–molybdenum alloys in an acidic chloride environment," *Corrosion Science*, vol. 52, no. 2, pp. 352–359, 2010. Available at: https://doi.org/10.1016/j.corsci.2009.09.021

[12] W. J. Botta, J. E. Berger, C. S. Kiminami, V. Roche, R. P. Nogueira, and C. Bolfarini, "Corrosion resistance of Fe-based amorphous alloys," *Journal of Alloys and Compounds*, vol. 586, pp. S105–S110, 2014. Available at: https://doi.org/10.1016/j.jallcom.2012.12.130

[13] S. Xie, J. Zhao, S. Li, and J. Su, "Enhanced mechanical properties of Zr-Cu-Al-Ni bulk amorphous alloys by Ag and O doping," *Journal of Alloys and Compounds*, vol. 957, p. 170186, 2023. Available at: https://doi.org/10.1016/j.jallcom.2023.170186

[14] T. W. Wilson, J. M. Bai, and H. Choo, "Enhanced thermal stability of amorphous aluminum alloys through microalloying," *Materials Letters*, vol. 62, no. 23, pp. 3790–3792, 2008. Available at: https://doi.org/10.1016/j.matlet.2008.03.063

[15] X. Xu, W. Li, B. Wan, S. Jin, K. Chen, and F. Su, "Extremely improved the corrosion resistance and anti-wear behavior of aluminum alloy in 3.5% NaCl solution via amorphous CrAlN coating protection," *Corrosion Science*, vol. 230, p. 111952, 2024. Available at: https://doi.org/10.1016/j.corsci.2024.111952

[16] X. Wang, Z. Ding, S. Li, and L. Peng, "Computation method for mechanical performances of die-cast aluminum alloys based on non-uniform material properties," *Materials Today Communications*, vol. 40, p. 109683, 2024. Available at: https://doi.org/10.1016/j.mtcomm.2024.109683

[17] H. Fan, J. Hu, Y. Wang, H. Zhang, W. Guo, J. Li, S. Xu, H. Li and P. Liu, "A review of laser additive manufacturing (LAM) aluminum alloys: Methods, microstructures and mechanical properties," *Optics & Laser Technology*, vol. 175, p. 110722, 2024. Available at: https://doi.org/10.1016/j.optlastec.2024.110722

[18] F. Han, C. Li, Y. Wang, Z. Pai, Y. Meng, M. Cao, Y. Liu, P. He, X. Ma, L. Xue and C. Wang, "Comparative study on corrosion property of 2219 aluminum alloy sheet and additively manufactured 2319 aluminum alloy," *Journal of Materials Research and Technology*, vol. 30, pp. 3178–3185, 2024. Available at: https://doi.org/10.1016/j.jmrt.2024.04.036

[19] H. Liu, J. Ying, Z. Chen, C. Ma, S. Qian, Y. Ouyang and X. Liu, "Research status of mechanical properties of aluminum alloy grid structure," *Structures*, vol. 61, p. 105967, 2024. Available at: https://doi.org/10.1016/j.istruc.2024.105967

[20] M. Pourbaix, *Atlas of electrochemical equilibria in aqueous solutions*, NACE International and Cebelcor, Houston, USA, 1974.

[21] L. C. R. Aliaga, C. R. M. Afonso, J. E. Spinelli, C. S. Kiminami, C. Bolfarini, and W. J. Botta, "Advanced characterization of Al–Ni-Sm amorphous alloys with dispersion of round Pb-rich nanoparticles," *Journal of Materials Research and Technology*, vol. 27, pp. 6892–6899, Oct. 2023. Available at: https://doi.org/10.1016/j.jmrt.2023.10.169

[22] F. G. Cuevas, S. Lozano-Perez, R. M. Aranda, and E. S. Caballero, "Crystallisation of amorphous Al-Sm-Ni-(Cu) alloys," *Intermetallic*s, vol. 112, p. 106537, 2019. Available at: https://doi.org/10.1016/j.intermet.2019.106537

[23] L. Li, J. Yang, and X. Shen, "Measuring the hydration product proportion in composite cement paste by using quantitative BSE-EDS image analysis: A comparative study" *Measurement*, vol. 199, p. 111290, May 2022. Available at: https://doi.org/10.1016/j.measurement.2022.111290

[24] P. M. Natishan and W. E. O'Grady, "Chloride ion with oxide-covered aluminum leading to pitting corrosion: A review," *Journal of the Electrochemical Society*, vol. 161, pp. C421-C432, 2014. Available at: https://doi.org/10.1149/2.1011409jes

[25] J. A. Moreto, C. E. B. Marino, W. W. B. Filho, L. A. Rocha, and J. C. S. Fernandes, "SVET, SKP and EIS study of the corrosion behaviour of high strength Al and Al–Li alloys used in aircraft fabrication," *Corrosion Science*, vol. 84, pp. 30–41, 2014. Available at: https://doi.org/10.1016/j.corsci.2014.03.001